



Cite this: *RSC Adv.*, 2018, 8, 39455

# Evaluation of residual stress and texture in isotope based $\text{Mg}^{11}\text{B}_2$ superconductor using neutron diffraction

Hyunseock Jie,<sup>ab</sup> Wenbin Qiu,<sup>a</sup> Daniel Gajda,<sup>id c</sup> Jeonghun Kim,<sup>id d</sup> Valiyaparambil Abdulsalam Anvar,<sup>id ae</sup> Arend Nijhuis,<sup>id e</sup> Yoshio Bando,<sup>af</sup> Yusuke Yamauchi,<sup>id \*dg</sup> Vladimir Luzin,<sup>id \*b</sup> and Md. Shahriar A. Hossain<sup>\*ah</sup>

Magnesium diboride ( $\text{MgB}_2$ ) superconducting wires have demonstrated commercial potential to replace niobium–titanium (NbTi) in terms of comparable critical current density. Its higher critical temperature makes  $\text{MgB}_2$  wire suitable for liquid-helium-free operation. We recently reported boron-11 isotope-based low-activation  $\text{Mg}^{11}\text{B}_2$  superconducting wire with decent critical current density appropriate for low-cost superconducting fusion magnets. In this study, we have mainly focused on the neutron diffraction technique to measure the residual stress in  $\text{Mg}^{11}\text{B}_2$  superconducting wire for the first time. The residual stress state was given qualitative and quantitative interpretation in terms of micro- and macrostress generation mechanisms based on the isotropic model confirmed by neutron texture measurements. The relationship between the stress/strain state in the wire and the transport critical current density is also discussed. This investigation could pave the way to further enhancement of the critical current density of low-activation  $\text{Mg}^{11}\text{B}_2$  superconducting wires suitable for next-generation fusion grade magnets.

Received 11th July 2018  
 Accepted 10th October 2018

DOI: 10.1039/c8ra05906c

[rsc.li/rsc-advances](http://rsc.li/rsc-advances)

## Introduction

While the current workhorse superconductors for the International Thermonuclear Experimental Reactor (ITER) are low-temperature NbTi and  $\text{Nb}_3\text{Sn}$  superconductors,<sup>1–3</sup>  $\text{MgB}_2$  shows electromagnetic performance superior to that of NbTi: it has lower induced radioactivity,<sup>4,5</sup> higher efficiency of the cryogenic reactor system,<sup>6–8</sup> and a much higher transition temperature ( $T_c$ ).<sup>9,10</sup> Furthermore, the field performance, in terms of its transport critical current density ( $J_c$ ) and upper critical field ( $B_{c2}$ ), is close to that of NbTi superconductor.<sup>11–13</sup> Thus,  $\text{MgB}_2$  is

possibly a viable candidate to replace NbTi superconductors in the poloidal field (PF) coils and correction coils (CC) for the next-generation fusion reactors. Based on the analysis reported by Devred *et al.* and Hossain *et al.* of the conductor development and performance criteria for the ITER project, the critical current capacity of  $\text{MgB}_2$  cables clearly fulfils the requirements for use in the PF and CC magnets, even at 20 K, in the ITER fusion reactor.<sup>13,14</sup> The use of conduction-cooled low-cost  $\text{MgB}_2$  at 20 K in PF and CC magnets to replace NbTi will make the next generation fusion reactor much more cost effective.  $\text{MgB}_2$  wire filament is brittle after the heat treatment, and given the strain limit criterion of 0.2% for the magnet design, the maximum strain limit is well below 0.2% to provide a factor of two safety margin.<sup>15</sup> Despite the prospects for the use of  $\text{MgB}_2$  as a fusion reactor superconducting material, many technological issues need to be resolved, and the current work aims to report the progress in this direction.

The critical point in reactor application is the use of boron-11 isotope enriched powder for the fabrication of the  $\text{MgB}_2$  superconductor. Natural boron has 19.78 wt% boron-10 ( $^{10}\text{B}$ ) and 80.22 wt% boron-11 ( $^{11}\text{B}$ ).<sup>16–18</sup>  $^{10}\text{B}$  is well known as a neutron absorption material with a large nuclear reaction cross-section, leading to transformation into  $^7\text{Li}$  and He *via* the ( $n, \alpha$ ) reaction.<sup>19–21</sup> In contrast,  $^{11}\text{B}$  is stable in the presence of neutron irradiation without an ( $n, \alpha$ ) reaction and can reduce nuclear heating.<sup>22,23</sup> Therefore,  $^{11}\text{B}$  isotope based  $\text{Mg}^{11}\text{B}_2$

<sup>a</sup>Australian Institute for Innovative Materials (AIIM), University of Wollongong, Squires Way, North Wollongong, NSW 2500, Australia. E-mail: shahriar@uow.edu.au

<sup>b</sup>Australian Nuclear Science & Technology Organisation (ANSTO), Lucas Heights, NSW 2232, Australia. E-mail: vll@ansto.gov.au

<sup>c</sup>Institute of Low Temperature and Structure Research Polish Academy of Sciences, ul. Okólna 2, 50-422 Wrocław, Poland

<sup>d</sup>School of Chemical Engineering, Australian Institute for Bioengineering and Nanotechnology (AIBN), The University of Queensland, Brisbane, QLD 4072, Australia. E-mail: y.yamauchi@uq.edu.au

<sup>e</sup>The University of Twente, Faculty of Science & Technology, 7522 NB Enschede, Netherlands

<sup>f</sup>International Center for Materials Nanoarchitectonics (WPI-MANA), National Institute for Materials Science (NIMS), 1-1 Namiki, Tsukuba, Ibaraki 305-0044, Japan

<sup>g</sup>Department of Plant & Environmental New Resources, Kyung Hee University, 1732 Deogyong-daero, Giheung-gu, Yongin-si, Gyeonggi-do 446-701, South Korea

<sup>h</sup>School of Mechanical and Mining Engineering, The University of Queensland, Brisbane, QLD 4072, Australia



superconductor is the most desirable, if not absolutely necessary, material for Tokamak type magnets in fusion reactors.

In recent ITER superconducting cable performance tests, damage to the superconducting filaments has been recognised as a significant issue.<sup>24</sup> It was demonstrated that the superconducting filaments in the cables are easily damaged when exposed to temperature and electromagnetic cycling, simulating ITER operational regimes, and that this microscale damage has a detrimental effect on superconducting properties. The root cause of the microscale damage is associated with electromagnetic (Lorentz) forces as well as thermally generated stresses due to cooling to cryogenic temperatures and residual stresses generated during the production process.<sup>25–28</sup> Therefore, it is essential to assess and, if possible, to control the stress and strain state of the filaments, both when it originates from the manufacturing process and when it occurs due to the operating conditions. This knowledge can be used to predict and, ideally, eliminate possible damage to the superconducting filaments. In this respect, the residual stress is not only a partial cause of the damage, but also a quantity that can be studied to assess the degree of microscale damage. In case of development of microscale damage, the residual stresses become relaxed to a certain degree, and this effect can be studied experimentally.

Knowledge of the residual stresses is also important for understanding the effects of applied stress/strain on the superconducting properties, *i.e.* the critical current ( $I_c$ ), which have been experimentally observed multiple times in  $MgB_2$  superconducting systems.<sup>29–32</sup> The residual stresses were measured successfully on several occasions for  $Nb_3Sn$  using neutron diffraction,<sup>33,34</sup> and this technique proved to be the most suitable for the powder-in-tube system due to its ability to penetrate through the sheath material. There are no published results on measurements of the residual stress in  $MgB_2$  wires, however, presumably due to the fact that manufacturing  $^{11}B$  isotope based  $Mg^{11}B_2$  wires is a prerequisite for such neutron measurements. Nevertheless, it is conceptually clear that, depending on the sign and magnitude of the residual stress, the combined effect of the residual and applied stress/strain can be different.

From this point of view, understanding the stress/strain behaviour of the  $Mg^{11}B_2$  wires and coils for the magnet system of a fusion reactor is a critical issue in terms of current-carrying capability. Direct stress/strain measurements on the  $Mg^{11}B_2$  filaments in the wire are difficult, because the  $Mg^{11}B_2$  filamentary region, for practical use, is covered with a Monel (Ni–Cu alloy) sheath and Nb barrier. A high penetration depth of radiation, such as in the form of neutrons or high-energy synchrotron X-rays, is required to measure residual stress and texture on the superconducting wire.<sup>35</sup>

In this report, we used neutron diffraction for a full quantitative residual stress analysis of the constituents in  $^{11}B$  isotope based  $Mg^{11}B_2$  wires ( $Mg^{11}B_2$ ), in correlation with the fabrication conditions and the transport critical current density ( $J_c$ ), for the first time. This assessment is the first step on the way to optimising the properties and manufacturing conditions for  $Mg^{11}B_2$  superconductor intended for magnets in fusion reactors, with the possibility of mitigating unwanted stress and strain inside the wire filaments.

## Experimental details

The wire samples were prepared by using the conventional *in situ* powder-in-tube (PIT) method. The  $^{11}B$  low crystalline powder (from Pavezyum Kimya, Turkey), which consists of amorphous and crystalline components, was sintered by the Moissan method<sup>36</sup> with 840 nm particle size and isotopic purity of  $99.25 \pm 0.01\%$  of  $^{11}B$ . Magnesium powder (100–200 mesh, 99% purity), a niobium barrier, and a Monel (Ni–Cu alloy) sheath tube were also used for the production of the  $Mg^{11}B_2$  wire. This particular  $^{11}B$  powder was chosen from a selection of several candidates on the basis of precursor powder and wire product characterisation (*e.g.* the isotopic purity reported above was determined by means of neutron transmission experiments and accelerator mass-spectrometry), and a study giving the details will be published separately elsewhere. The tube was swaged and drawn to an outer diameter of 1.08 mm, and then the wires were subjected to heat treatment at 700 °C, 750 °C, and 800 °C for 1 hour (ramp rate of 5 °C min<sup>-1</sup>) under a high purity argon gas atmosphere. Scanning electron microscopy (SEM, JEOL JSM-6490LV) and X-ray diffraction (XRD, GBC-MMA) were employed to observe the microstructure and the phase composition using sectioned wires. The core,  $Mg^{11}B_2$  based ceramic, was extracted from the Nb-Monel sheath for the X-ray diffraction. The volume fractions of  $^{11}B$ -rich phase, Mg, and MgO for  $Mg^{11}B_2$  were obtained using the MAUD program based on the X-ray diffraction.<sup>37–41</sup>

For neutron experiments, the individual  $Mg^{11}B_2$  wires were cut into pieces ~5 mm in length and bunched together to form bulk samples with approximate dimensions of  $5 \times 5 \times 5$  mm<sup>3</sup>. Measurements of residual stress were performed on the niobium,  $Mg^{11}B_2$ , and Monel phases. The measurements of residual stress on the  $Mg^{11}B_2$  wires were carried out using the KOWARI neutron diffractometer<sup>42</sup> at the Open Pool Australian Lightwater (OPAL) research reactor at the Australian Nuclear Science and Technology Organization (ANSTO). The  $Mg^{11}B_2$  phase was measured in a 90° geometry using the wavelength  $\lambda = 1.5$  Å for the  $Mg^{11}B_2$  (211) reflection and gauge volume size of  $4 \times 4 \times 4$  mm<sup>3</sup>. Two principal directions, transverse and axial, were measured with constant rotation of the samples around their axis for better averaging.

A specially prepared pure  $Mg^{11}B_2$  cylindrical pellet sample (5 mm diameter, 3 mm height) was used to determine the unstressed lattice spacing,  $d_0$ . For the production of this pellet, a high temperature (HT) 800 °C thermal regime was used to produce a uniform (no Monel sheath, no Nb barrier) and high purity sample to ensure the absence of macro- and microstresses.

The stress ( $\sigma$ ) was calculated for the measured transverse and axial strains,  $\epsilon_t = (d_t - d_0)/d_0$  and  $\epsilon_a = (d_a - d_0)/d_0$ , respectively, of the  $Mg^{11}B_2$  (211) reflections in the corresponding directions using the (*hkl*)-dependent Young's modulus ( $E$ ) and Poisson's ratio ( $\nu$ ) calculated from the single crystal elastic constants in the isotropic approximation,  $E(211) = 316.2$  GPa, and  $\nu(211) = 0.17$ . The two principal stress components, transverse and axial, were computed accordingly to the following relationship



$\sigma_{a,t} = \frac{E}{1+\nu} \{ \varepsilon_{a,t} + \frac{\nu}{1-2\nu} (\varepsilon_a + 2\varepsilon_t) \}$  adapted for the case of the cylindrical symmetry stress state from the general Hooke's law.<sup>43,44</sup> The cylindrical symmetry of the stress state reflects and inherits the cylindrical symmetry of the wire drawing process with only two distinct directions, axial and transverse.

To further study aspects of the anisotropic stress state, neutron texture measurements were performed on the wires, including three phases, Mg<sup>11</sup>B<sub>2</sub>, Monel sheath, and Nb barrier (only for the sample sintered at 700 °C, since the other samples were essentially identical). Several representative pole figures were collected to judge the crystallographic isotropy/anisotropy using the same KOWARI diffractometer. We consider that the effect of crystallographic texture,<sup>45</sup> which requires experimental determination, is three fold. First, it determines the anisotropy of the elastic and thermal properties (*e.g.* Young's modulus and the coefficient of thermal expansion), which is important for proper stress calculation procedures, as well as for stress evaluation if a finite element method (FEM) simulation is to be done. Second, if some crystallographic preferred orientation is found, it can shed light on the mechanism of MgB<sub>2</sub> phase formation and growth in the sintering process. Third, for the polycrystalline layered superconductors, *e.g.* yttrium barium copper oxide (YBCO), with extremely high anisotropy of the critical current, the effect of texture is so high that the current can be practically destroyed due to unfavourable crystallographic alignment of the grains.<sup>46</sup> Although the single crystal anisotropy of MgB<sub>2</sub> is much less pronounced, control of the degree of preferred orientation is required.

## Results and discussion

The crystallographic anisotropy was quantified by neutron texture analysis, and the results are shown in Fig. 1 as a set of representative pole figures for the three materials used in the wire, Monel, Nb, and Mg<sup>11</sup>B<sub>2</sub>.<sup>45</sup> While there is strong anisotropy in the Monel-Nb sheath due to tensile plastic deformation during the swaging process, the crystal orientation of Mg<sup>11</sup>B<sub>2</sub> has a random distribution (with only statistical oscillations visible in the pole figures of Mg<sup>11</sup>B<sub>2</sub>, while there is no pattern with preferred orientation). Thus Mg<sup>11</sup>B<sub>2</sub> phase is crystallographically isotropic (with no preferred crystal orientation), and therefore, the elastic properties, which are important for the stress analysis of the system, have no anisotropy related to the crystalline preferred orientation. This does not eliminate the possibility of elastic anisotropy due to other micromechanical factors, however, *e.g.* microcracking determined, for example, by the deformation process. The results of the texture analysis are to be used for macrostress calculations in the elastically anisotropic model of the sheath material and its interaction with the Mg<sup>11</sup>B<sub>2</sub> interior, which is isotropic. The experimentally determined isotropy of the Mg<sup>11</sup>B<sub>2</sub> interior is used here for model microstress calculations within the isotropic approximation.

Fig. 2(a) shows that the cross-sectional microstructure of the wire consists of 49 vol% Monel, 28 vol% Nb, and 23 vol% Mg<sup>11</sup>B<sub>2</sub>. Fig. 2(b) presents the XRD patterns of the

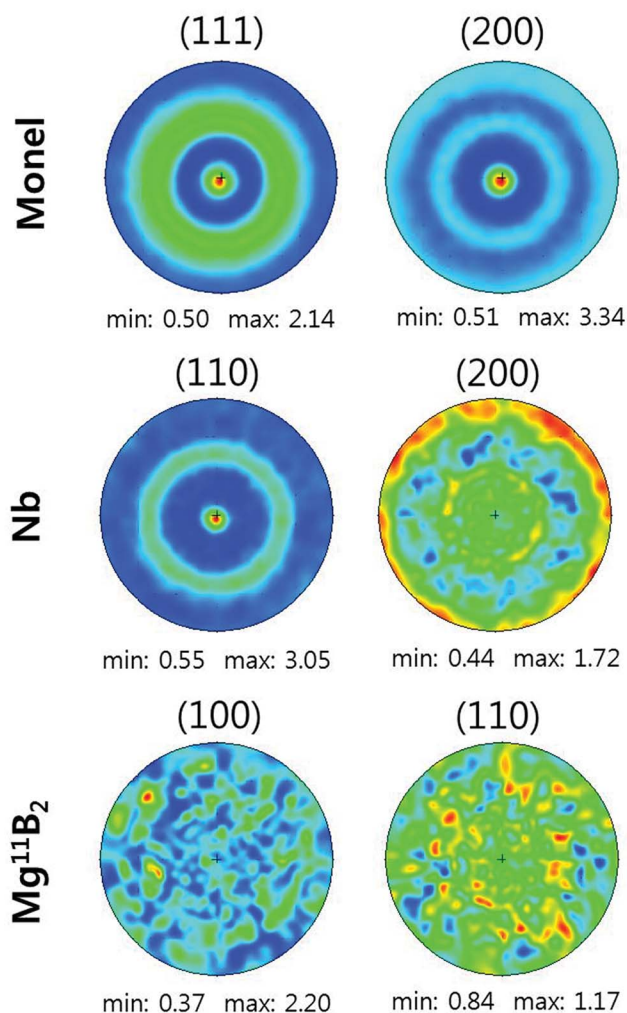


Fig. 1 Pole figures of the phases in the Mg<sup>11</sup>B<sub>2</sub> wire heat-treated at 700 °C.

superconducting ceramic from the core of the Mg<sup>11</sup>B<sub>2</sub> wires after sintering for one hour at 700 °C, 750 °C, and 800 °C. While the major peaks are indexed as Mg<sup>11</sup>B<sub>2</sub> phase, unreacted Mg, MgO, and <sup>11</sup>B-rich phase<sup>47,48</sup> are present in the samples. Fig. 2(c) shows the volume fractions of the secondary phases as functions of the sintering temperature. In the wires sintered at 700 °C and 750 °C, there are certain amounts of retained <sup>11</sup>B-rich phase and Mg phase, 10–20 vol%, sufficient to produce significant and measurable microstresses. Further increasing the heat-treatment to 800 °C diminished the volume fraction of the Mg and the <sup>11</sup>B rich phase to 0.37% and 0.47%, respectively, resulting in the most fully reacted, most pure Mg<sup>11</sup>B<sub>2</sub> superconductor.

Fig. 3 shows the experimental results for the residual stress measurements of Mg<sup>11</sup>B<sub>2</sub> wires in the transverse and the axial directions, with error bars showing the estimated uncertainty due to neutron counting statistics. The wires were characterised to have tensile stress of 66 ± 15 MPa (HT 700 °C), 50 ± 15 MPa (HT 750 °C), and 6 ± 15 MPa (HT 800 °C) for the transverse component, which had a tendency to decrease with increasing





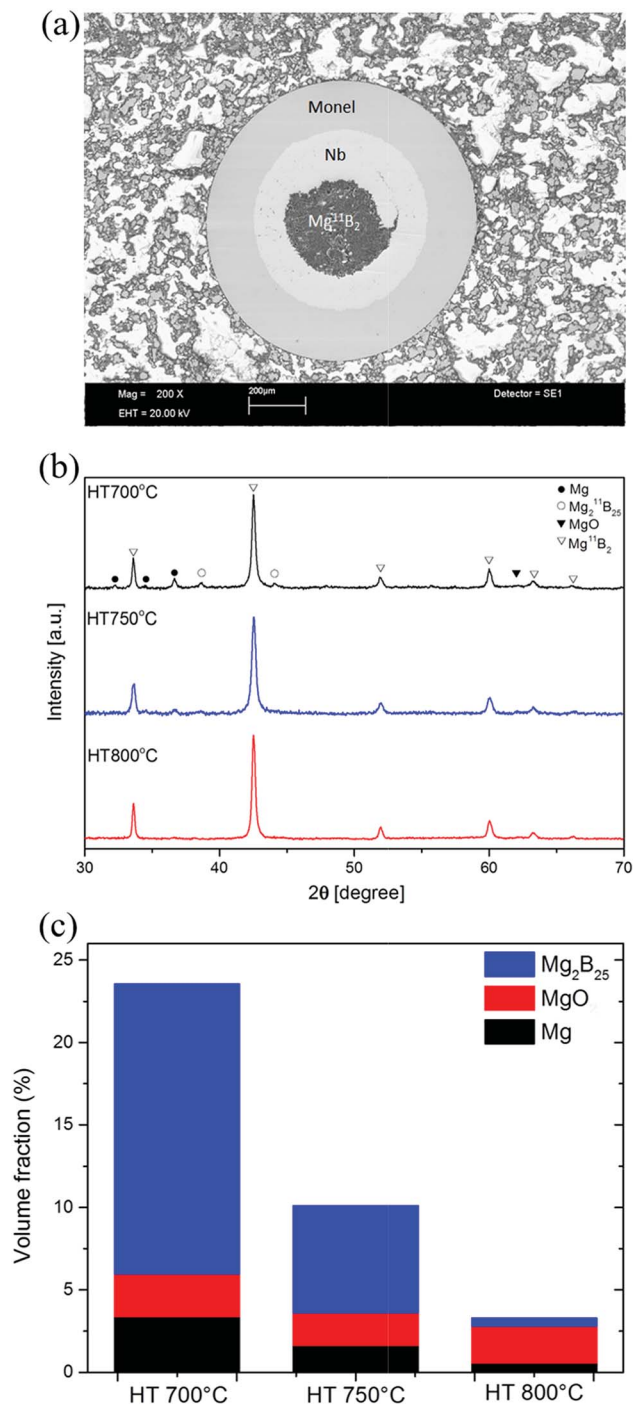


Fig. 2 (a) The cross-sectional microstructure is shown in an SEM image of the Monel, Nb, and  $Mg^{11}B_2$ ; (b) XRD patterns of the interior material of the  $Mg^{11}B_2$  wires (Monel and Nb barrier are removed) after heat-treatment at 700 °C, 750 °C, and 800 °C; (c) the volume fractions of boron-rich phase ( $Mg_2B_{25}$ ), Mg, and MgO for  $Mg^{11}B_2$  produced under different heat-treatment conditions.

heat-treatment temperature to almost negligible in the HT 800 °C sample.

The approach of the stress analysis and interpretation is based on the decomposition of the total stress into micro- and macro-stress.<sup>49</sup> In the given system it is deemed that both components are present due to the structure of the wire, there is

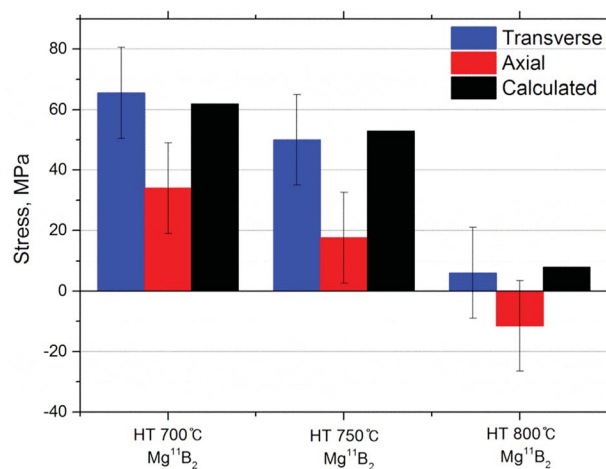


Fig. 3 Residual stress in the  $Mg^{11}B_2$  wires heat-treated at 700 °C, 750 °C, and 800 °C.

an inner core, which is by itself is a composite material, and there is also a possible interaction between that core and our metal sheath.

The main contribution to the total stress was hydrostatic microstress (phase incompatibility stress) due to the interaction between the  $Mg^{11}B_2$  matrix and the elastically harder  $^{11}B$  rich phase upon cooling down from the sintering temperature.<sup>50</sup> It is generated due to the difference in the thermal expansion of the phases. This microstress is assumed fully thermally generated, since  $MgB_2$  phase is synthesised during the heat-treatment process, and isotropic, since all constituent phases are crystallographically isotropic. This experimental result was corroborated by evaluating thermally generated phase stresses using a micromechanical model of the isotropic particulate composite based on the Eshelby inclusion formalism.<sup>51,52</sup> The calculations were made accordingly to the evaluated volume fractions (Fig. 2) of the constituents ( $Mg^{11}B_2$  as the primary phase, plus unreacted  $^{11}B$  rich phase inclusions) and the thermal conditions for the composite formation in the Mg-B phase diagram.<sup>53</sup> A good numerical agreement with the experimental results was achieved. (Fig. 3 combines the experimental and calculated results.) Thus, based on the XRD phase analysis results and the residual stress neutron measurements, it can be concluded that the higher heat-treatment temperature of 800 °C is required for the full reaction of the  $^{11}B$  rich and Mg phases to form  $Mg^{11}B_2$ , which ensures a low level of residual microstress.

In the axial direction, some compressive contribution to the total stress is present in addition to the hydrostatically-compressive microstress contribution discussed above, thus bringing the stress in the axial direction from tensile to less tensile, or even into compressive range, as in the 800 °C heat-treated wire. This effect can be explained by the interaction between the Monel-Nb sheath and the  $Mg^{11}B_2$ , and is due to thermally generated macrostress. Taking account of the differences in the coefficient of thermal expansion (CTE) of the sheath and wire interior ( $\Delta\alpha$ ) and the temperature drop from the sintering temperature to room temperature ( $\Delta T$ ), the thermal strain mismatch  $\Delta\epsilon = \Delta T \cdot \Delta\alpha$  determines the sign and



magnitude of the macrostress in the sheath and in the interior of the wire. Based on the CTEs of the constituents,  $\alpha(\text{Mg}^{11}\text{B}_2) = 8.3 \times 10^{-6}/\text{K}$ ,<sup>54</sup>  $\alpha(\text{Monel}) = 14 \times 10^{-6}/\text{K}$ ,<sup>55</sup> and  $\alpha(\text{Nb}) = 7.3 \times 10^{-6}/\text{K}$ ,<sup>56</sup> a compressive axial stress should be generated in  $\text{Mg}^{11}\text{B}_2$ , compensated by the tensile stress in the Monel sheath. In the wires sintered at 700 °C and 750 °C, with some amount of unreacted Mg phase and  $^{11}\text{B}$  rich phase, the same consideration is supposed to include Mg ( $\alpha = 24.8 \times 10^{-6}/\text{K}$ )<sup>57</sup> and  $^{11}\text{B}$  ( $\alpha = 6 \times 10^{-6}/\text{K}$ )<sup>58</sup> as well as microstructure features (*e.g.* possible pores and cracking). The resultant effect is highly sensitive to the conditions on the contact between the Monel tube and the  $\text{Mg}^{11}\text{B}_2$  composite interior. Yet another explanation of this partial stress relaxation in the axial direction could be the presence of oriented cracks and pores arising from contraction during the sintering process and the pores originating from the  $\text{Mg}^{11}\text{B}_2$  phase formation reaction in the heat-treatment procedure.

Fig. 4(a–d) shows the microstructure in the longitudinal direction of the  $\text{Mg}^{11}\text{B}_2$  wires sintered at 700 °C, 750 °C, and 800 °C. These secondary electron image (SEI) observations indicate that aggregation occurs along with the presence of some small pores and microcracks in the 700 °C and 750 °C wires (Fig. 4(a and b)), while cracking and pores are more pronounced in the wire heat-treated at 800 °C (Fig. 4(c and d)). As the heat-treatment temperature increases, the aggregation of the  $\text{Mg}^{11}\text{B}_2$  growth proceeds continuously while creating pores. As a result of the aggregation,  $\text{Mg}^{11}\text{B}_2$  has a porous structure, and it can be easily damaged by thermal stress caused by the temperature drop from above 700 °C to room temperature.

Although the pores provide a precondition for the cracking-susceptible microstructure, the actual origin and mechanism

of stress generation is twofold. First, due to the difference in CTE between the Monel/Nb sheath and the superconducting material, macrostress is generated, which in circumstances of porous microstructure leads to stress concentration. Second, due to the anisotropic thermal expansion of  $\text{Mg}^{11}\text{B}_2$  (hexagonal crystal structure,  $\alpha(a) = 5.4 \times 10^{-6}/\text{K}$ ,  $\alpha(c) = 11.4 \times 10^{-6}/\text{K}$  (ref. 59)), when the grains are randomly oriented, microstresses can also be generated. Although the overall average volume of these stresses is zero, the localised stresses can reach very large values, up to  $\sim 1$  GPa accordingly to our estimates. Thus, through these thermal mechanisms, very high magnitude and locally concentrated stress fields are generated, leading to microcrack formation conditions. The exact morphology, phase composition, and other details of the microstructure play roles in the actual stress state of the superconducting material. Thus, the more porous structure of the 800 °C sample makes it more cracking-prone than the lower temperature samples (700 °C and 750 °C) with more homogeneous structures. Also, while in less pure samples (700 °C and 750 °C), the local stress/strain fields can be accommodated by the plastically soft metallic Mg phase, this mechanism is substantially suppressed in the most pure (800 °C) sample, and thus, cracks are more easily formed in the 800 °C sample. Therefore, due to these two mechanisms, the most significant cracks on the scale of several microns are formed in the 800 °C sample.

Furthermore, the brittle fracturing leads to extensive cracking in the  $\text{Mg}^{11}\text{B}_2$  structure, as seen in Fig. 4(c and d), resulting in a harmful effect on the transport  $J_c$  properties in  $\text{Mg}^{11}\text{B}_2$  wire.<sup>60,61</sup> In fact, it was previously reported in our research results that the wire sintered at 800 °C did not show

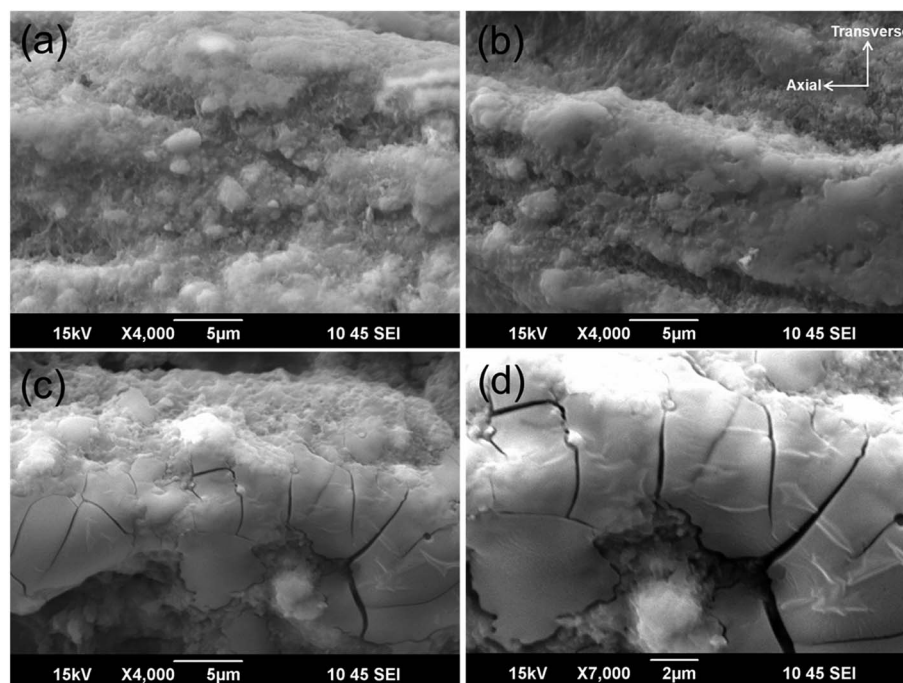


Fig. 4 Low-vacuum SEM images of longitudinal sections of  $\text{Mg}^{11}\text{B}_2$  wires heat-treated at (a) 700 °C, (b) 750 °C, and (c and d) 800 °C.



a transport  $J_c$ , even though the sample was fully reacted with a high  $\text{Mg}^{11}\text{B}_2$  superconducting phase fraction.<sup>62</sup> On the other hand, the wire sintered at 750 °C has a superior transport critical current density,  $J_c = 2 \times 10^4 \text{ A cm}^{-2}$  at 4.2 K and 5 T compared with the multifilament wire manufactured by the National Institute for Fusion Science (NIFS).<sup>62</sup> Therefore, based on the above discussion, the cracks and the pores have a detrimental influence on  $J_c$  through fracturing of the inter-grain connections, while, at the same time, these defects act as stress relief factors in the  $\text{Mg}^{11}\text{B}_2$  wire sintered at 800 °C.

The superconducting transition temperature ( $T_c$ ) was observed at a temperature of 36.5 K and 36.9 K, for the samples sintered at 700 °C and 800 °C, respectively.<sup>62</sup> Compared to the reported results, *e.g.* 39.2 K in,<sup>63</sup> the lower  $T_c$  in the present samples is most likely due to the presence and complex interactions of different types of  $\text{MgB}_2$  lattice defects, such as lattice strains/stresses, poor crystallinity, the presence of point defects and defects with higher dimensions, and issues with chemical purity and phase purity (*e.g.* the presence of small amounts of  $\text{MgO}$ ).<sup>64</sup> The exact role of each factor might be difficult to address, however due to the intertwined nature of these mechanisms.<sup>65</sup>

## Conclusion

Due to its relevance to the superconducting properties, the stress state of  $\text{Mg}^{11}\text{B}_2$  wires sintered (heat-treated) at different temperatures was investigated using neutron diffraction. We found that the stress in  $\text{Mg}^{11}\text{B}_2$  is due to two contributions: one is the thermally generated hydrostatic microstress most clearly manifested in the transverse direction; the other is the contribution of the thermally generated macrostress, which has a uniaxial nature due to the “wire sheath-interior” interaction with its effects in the axial direction and/or possibly some contribution to stress relaxation due to oriented microcracking. We also found that, as the sintering temperature increases to 800 °C, it leads to the formation and growth of cracks in the superconducting ceramic as well as presence of some pores. These defects are, most likely, not related to the thermally generated stress, in so far as it is the lowest in the 800 °C sintered sample, but initiated during the sintering process itself and most likely involving the phase transformation mechanism. The extended cracking negatively affects the superconducting properties in the  $\text{Mg}^{11}\text{B}_2$  wire, to the point of total loss of the superconductivity, even though the  $\text{Mg}^{11}\text{B}_2$  superconducting ceramic sintered at 800 °C is the most pure and would be expected to have better properties because the high sintering temperature gives rise to stress relief in the  $\text{Mg}^{11}\text{B}_2$  wire. In other words, the noticeable relaxation of the residual stresses in the axial and the transverse directions implies that the poor transport  $J_c$  value is caused by insufficient grain connection in the  $\text{Mg}^{11}\text{B}_2$  wire. Overall, the micromechanical and structural features of the  $\text{Mg}^{11}\text{B}_2$ -based wires are essential for their performance, and neutron diffraction seems to be an appropriate analytical tool for assessment of the residual stress state as well as the crystallographic anisotropy (texture).

## Author contributions

H. J. and W. Q. prepared the samples, V. A. A., A. N. and Y. B. characterized the samples, D. G., J. K. and Y. Y. contributed to discussions on the obtained data, and V. L. and M. S. A. H. organized the manuscript.

## Conflicts of interest

The authors declare no competing financial interests.

## Acknowledgements

This work was supported by the Australian Centre for Neutron Scattering (ACNS) through its user access program (Proposals 3544 and 5436). This work was also supported by the Australian Research Council (Grant No. LP160101784). The authors acknowledge the use of facilities within the UOW Electron Microscopy Centre. This work was performed in part at the Queensland node of the Australian National Fabrication Facility, a company established under the National Collaborative Research Infrastructure Strategy to provide nano- and micro-fabrication facilities for Australia's researchers.

## References

- 1 A. Devred, *et al.*, Challenges and status of ITER conductor production, *Supercond. Sci. Technol.*, 2014, **27**, 044001.
- 2 T. Boutboul, *et al.*, Status of the Procurement of the European Superconductors for the ITER Magnets, *IEEE Trans. Appl. Supercond.*, 2014, **24**, 6001004.
- 3 N. Mitchell and A. Devred, The ITER magnet system: Configuration and construction status, *Fusion Eng. Des.*, 2017, **123**, 17–25.
- 4 T. Noda, T. Takeuchi and M. Fujita, Induced activity of several candidate superconductor materials in a tokamak-type fusion reactor, *J. Nucl. Mater.*, 2004, **329–333**, 1590–1593.
- 5 B. A. Glowacki and W. J. Nuttall, Assessment of liquid hydrogen cooled  $\text{MgB}_2$  conductors for magnetically confined fusion, *J. Phys.: Conf. Ser.*, 2008, **97**, 012333.
- 6 W. Yao, *et al.*, A Solid Nitrogen Cooled  $\text{MgB}_2$  “Demonstration” Coil for MRI Applications, *IEEE Trans. Appl. Supercond.*, 2008, **18**, 912–915.
- 7 M. Tomsic, *et al.*, Overview of  $\text{MgB}_2$  Superconductor Applications, *Int. J. Appl. Ceram. Technol.*, 2007, **4**, 250–259.
- 8 Y. Iwasa, Towards liquid-helium-free, persistent-mode  $\text{MgB}_2$  MRI magnets: FBML experience, *Supercond. Sci. Technol.*, 2017, **30**, 053001.
- 9 J. Nagamatsu, *et al.*, Superconductivity at 39 K in magnesium diboride, *Nature*, 2001, **410**, 63–64.
- 10 C. Buzea and T. Yamashita, Review of the superconducting properties of  $\text{MgB}_2$ , *Supercond. Sci. Technol.*, 2001, **14**, 115–146.
- 11 D. Patel, *et al.*, Rational design of  $\text{MgB}_2$  conductors towards practical applications, *Cryogenics*, 2014, **63**, 160.





- 12 D. Wang, *et al.*, Transport properties of multifilament MgB<sub>2</sub> long wires and coils prepared by an internal Mg diffusion process, *Supercond. Sci. Technol.*, 2017, **30**, 064003.
- 13 M. S. A. Hossain, *et al.*, The roles of CHPD: Superior critical current density and n-value obtained in binary *in situ* MgB<sub>2</sub> cables, *Supercond. Sci. Technol.*, 2014, **27**, 095016.
- 14 A. Devred, *et al.*, Status of ITER Conductor Development and Production, *IEEE Trans. Appl. Supercond.*, 2012, **22**, 4804909.
- 15 T. Baig, *et al.*, Conceptual designs of conduction cooled MgB<sub>2</sub> magnets for 1.5 and 3.0 T full body MRI systems, *Supercond. Sci. Technol.*, 2017, **30**, 043002.
- 16 T. Ogitsu, E. Schwegler and G. Galli,  $\beta$ -Rhombohedral Boron: At the Crossroads of the Chemistry of Boron and the Physics of Frustration, *Chem. Rev.*, 2013, **113**, 3425–3449.
- 17 L. Chkhartishvili, Isotopic effects of boron (Review), *Trends Inorg. Chem.*, 2009, **11**, 105–167.
- 18 V. F. Sears, Neutron scattering lengths and cross sections, *Neutron News*, 1992, **3**, 26–37.
- 19 M. Eisterer, *et al.*, Neutron irradiation of MgB<sub>2</sub> bulk superconductors, *Supercond. Sci. Technol.*, 2002, **15**, L9–L12.
- 20 R. H. T. Wilke, S. L. Bud'ko and P. C. Canfield, Systematic study of the superconducting and normal-state properties of neutron-irradiated MgB<sub>2</sub>, *Phys. Rev. B: Condens. Matter Mater. Phys.*, 2006, **73**, 134512.
- 21 M. Putti, *et al.*, Neutron irradiation of Mg<sup>11</sup>B<sub>2</sub>: from the enhancement to the suppression of superconducting properties, *Appl. Phys. Lett.*, 2005, **86**, 112503.
- 22 F. P. Mooring, J. E. Monahan and C. M. Huddleston, Neutron cross sections of the boron isotopes for energies between 10 and 500 keV, *Nucl. Phys.*, 1966, **82**, 16–32.
- 23 F. Cheng, *et al.*, Improved superconducting properties in the Mg<sup>11</sup>B<sub>2</sub> low activation superconductor prepared by low-temperature sintering, *Sci. Rep.*, 2016, **6**, 25498.
- 24 N. Mitchell, *et al.*, Reversible and irreversible mechanical effects in real cable-in-conduit conductors, *Supercond. Sci. Technol.*, 2013, **26**, 114004.
- 25 A. Nijhuis, A solution for transverse load degradation in ITER Nb<sub>3</sub>Sn CICC: Verification of cabling effect on Lorentz force response, *Supercond. Sci. Technol.*, 2008, **21**, 054011.
- 26 V. Arp, Stresses in superconducting solenoids, *J. Appl. Phys.*, 1977, **48**, 2026–2036.
- 27 H. Bajas, D. Durville, D. Ciazynski and A. Devred, Approach to Heterogeneous Strain Distribution in Cable-In-Conduit Conductors Through Finite Element Simulation, *IEEE Trans. Appl. Supercond.*, 2012, **22**, 4803104.
- 28 K. Osamura, *et al.*, Local strain and its influence on mechanical–electromagnetic properties of twisted and untwisted ITER Nb<sub>3</sub>Sn strands, *Supercond. Sci. Technol.*, 2012, **25**, 054010.
- 29 H. Kitaguchi, H. Kumakura and K. Togano, Strain Effect in MgB<sub>2</sub>/Stainless Steel Superconducting Tape, *Phys. C*, 2001, **363**, 198–201.
- 30 H. Kitaguchi and H. Kumakura, Superconducting and mechanical performance and the strain effects of a multifilamentary MgB<sub>2</sub>/Ni tape, *Supercond. Sci. Technol.*, 2005, **18**, S284–S289.
- 31 K. Katagiri, *et al.*, Stress–strain effects on powder-in-tube MgB<sub>2</sub> tapes and wires, *Supercond. Sci. Technol.*, 2005, **18**, S351–S355.
- 32 G. Nishijima, *et al.*, Mechanical properties of MgB<sub>2</sub> superconducting wires fabricated by internal Mg diffusion process, *Supercond. Sci. Technol.*, 2012, **25**, 054012.
- 33 S. Harjo, *et al.*, Residual Strains in ITER Conductors by Neutron Diffraction, *Mater. Sci. Forum*, 2014, **777**, 84–91.
- 34 C. Scheuerlein, *et al.*, Residual strain in the Nb<sub>3</sub>Sn 11 T dipole magnet coils for HL-LHC, *Supercond. Sci. Technol.*, 2017, **30**, 125002.
- 35 M. T. Hutchings, P. J. Withers, T. M. Holden and T. Lorentzen, *Introduction to the Characterization of Residual Stress by Neutron Diffraction*, Taylor & Francis, Boca Raton London New York Singapore, 2005, pp. 1–272.
- 36 L. Y. Markovskii, Chemistry of magnesiothermal preparation of boron, *Electron Technol.*, 1970, **3**, 95–102.
- 37 L. Lutterotti, S. Matthies and H.-R. Wenk, *MAUD (Material Analysis Using Diffraction) Program*, available from: <http://maud.radiographema.eu/>, 2017.
- 38 G. V. Raynor and W. Hume-Rothery, A technique for the X-ray powder photography of reactive metals and alloys with special reference to the lattice spacing of magnesium at high temperatures Locality, *J. Inst. Met.*, 1939, **65**, 477–485.
- 39 L. Bindi, A. Figini Atti, G. Giunchi, L. Malpezzi and M. Norberto Lutterotti, Redetermination of Mg<sub>2</sub>B<sub>25</sub> based on single-crystal X-ray data, *Acta Crystallogr., Sect. E: Struct. Rep. Online*, 2012, **68**, i50.
- 40 S. Sasaki, K. Fujino and Y. Takeuchi, X-Ray Determination of Electron-Density Distributions in Oxides, MgO, MnO, CoO, and NiO, and Atomic Scattering Factors of their Constituent Atoms, *Proc. Jpn. Acad., Ser. B*, 1979, **55**, 43–48.
- 41 [https://materials.springer.com/isp/crystallographic/docs/sd\\_1815267](https://materials.springer.com/isp/crystallographic/docs/sd_1815267).
- 42 O. Kirstein, V. Luzin and U. Garbe, The Strain-Scanning Diffractometer Kowari, *Neutron News*, 2009, **20**, 34–36.
- 43 E. Kröner, Elastic moduli of perfectly disordered composite materials, *J. Mech. Phys. Solids*, 1967, **15**, 319–329.
- 44 M. T. Hutchings, P. J. Withers, T. M. Holden and T. Lorentzen, *Introduction to the Characterization of Residual Stress by Neutron Diffraction*, Taylor & Francis, Boca Raton London New York Singapore, 2005, pp. 213–273.
- 45 C. N. Tomé, H. R. Wenk and U. F. Kocks, *Texture and Anisotropy: Preferred Orientations in Polycrystals and Their Effect on Materials Properties*, Cambridge University Press, 2000.
- 46 H. Hilgenkamp and J. Mannhart, Grain boundaries in high T<sub>c</sub> superconductors, *Rev. Mod. Phys.*, 2002, **74**, 485–549.
- 47 A. G. Bhagurkar, *et al.*, Microstructural evolution in infiltration-growth processed MgB<sub>2</sub> bulk superconductors, *J. Am. Ceram. Soc.*, 2017, **100**, 2451–2460.
- 48 G. Giunchi, C. Orecchia, L. Malpezzi and N. Masciocchi, Analysis of the minority crystalline phases in bulk superconducting MgB<sub>2</sub> obtained by reactive liquid Mg infiltration, *Phys. C*, 2006, **433**, 182–188.



- 49 M. T. Hutchings and A. D. Krawitz, *Measurement of Residual and Applied Stress using Neutron Diffraction*, Series E: Applied Sciences, 1991, vol. 216.
- 50 G. Giunchi, T. Cavallin, P. Bassani and S. Guicciardi, The mechanical properties of the MgB<sub>2</sub> bulk materials obtained by reactive liquid Mg infiltration, *AIP Conf. Proc.*, 2008, **986**, 396–404.
- 51 J. D. Eshelby, The determination of the elastic field of an ellipsoidal inclusion and related problems, *Proc. R. Soc. London*, 1957, **A241**, 376–396.
- 52 J. D. Eshelby, The Elastic Field outside an Ellipsoidal Inclusion, *Proc. R. Soc. London*, 1959, **A252**, 561–569.
- 53 T. B. Massalski, H. Okamoto, P. R. Subramanian and L. Kacprzak, *Binary Alloy Phase Diagrams*, ASM International, 1990.
- 54 W. Goldacker, S. I. Schlachter, S. Zimmer and H. Reiner, High transport currents in mechanically reinforced MgB<sub>2</sub> wires, *Supercond. Sci. Technol.*, 2001, **14**, 787–793.
- 55 National Bureau of Standards Publications (U.S.), *Thermal expansion of nickel, Monel metal, Stellite, stainless steel, and aluminium*, Scientific Papers of the Bureau of Standards, vol. 17, 1921, pp. 497–519.
- 56 F. Cverna, *ASM Ready Reference: Thermal Properties of Metals*, ASM International 06702G, 2002, pp. 9–13.
- 57 D. L. Perry and S. L. Phillips, *Handbook of Inorganic Compounds*, CRC Press, 1995, p. 234.
- 58 C. E. Holcombe Jr, *et al.*, Physical-Chemical Properties of beta-Rhombohedral Boron, *High Temp. Sci.*, 1973, **5**, 349–357.
- 59 J. D. Jorgensen, D. G. Hinks and S. Short, Lattice Properties of MgB<sub>2</sub> versus Temperature and Pressure, *Phys. Rev. B: Condens. Matter Mater. Phys.*, 2001, **63**, 224522.
- 60 C. H. Jiang, H. Kumakura and S. X. Dou, Enhancement of the low-field  $J_c$  properties of MgB<sub>2</sub>/Fe tapes by a modified *in situ* process, *Supercond. Sci. Technol.*, 2007, **20**, 1015–1018.
- 61 Y. Liu, F. Xue and X. Gou, The Influence of Dispersedly Distributed Cracks on Critical Current of the Nb<sub>3</sub>Sn Strand, *J. Supercond. Novel Magn.*, 2017, 1–6.
- 62 W. Qiu, *et al.*, Improvement in the transport critical current density and microstructure of isotopic Mg<sup>11</sup>B<sub>2</sub> monofilament wires by optimizing the sintering temperature, *Sci. Rep.*, 2016, **6**, 36660.
- 63 S. Margadonna, *et al.*, Phase inhomogeneities and lattice expansion near  $T_c$  in the Mg<sup>11</sup>B<sub>2</sub> superconductor, *J. Phys.: Condens. Matter*, 2001, **13**, L795–L802.
- 64 J. H. Kim, *et al.*, The effects of sintering temperature on superconductivity in MgB<sub>2</sub>/Fe wires, *Supercond. Sci. Technol.*, 2007, **20**, 448–451.
- 65 R. Flükiger, *MgB<sub>2</sub> Superconducting Wires, Basics and Applications*, World Scientific, 2016.

